Atmospheric and Terrain Factors Influencing Martian Dust Devils.

Quentin N. Betton, *Nantes Université, Univ Angers, Le Mans Université, CNRS, Laboratoire de Planétologie et Géosciences, LPG UMR 6112, France (quentin.betton@etu.univ-nantes.fr)*, **Susan J. Conway,** *Nantes Université, Univ Angers, Le Mans Université, CNRS, Laboratoire de Planétologie et Géosciences, LPG UMR 6112, France (susan.conway@univ-nantes.fr)*, **Valentin T. Bickel,** *Center for Space and Habitability, University of Bern, Switzerland (valentin.bickel@unibe.ch)*, **Lori K. Fenton,** *Carl Sagan Center, SETI Institute, USA (lfenton@carlsagancenter.org)*, **Manish R. Patel,** *Sch. of Physical Sciences, The Open University, UK (manish.patel@open.ac.uk)*, **Helen C. Carson,** *Dept. of Materials Science & Engineering, University of Washington, WA, USA (helen@jimcarson.com)*, **Antoine Blouin,** *Nantes Université, Univ Angers, Le Mans Université, CNRS, Laboratoire de Planétologie et Géosciences, LPG UMR 6112, France (antoine.blouin@oca.eu)*, **Justin Crevier,** *Dept. of Physics, Boise State University, Boise, Idaho, USA (justincrevier@u.boisestate.edu)*, **Evan Blanc,** *Nantes Université, Univ Angers, Le Mans Université, CNRS, Laboratoire de Planétologie et Géosciences, LPG UMR 6112, France (evan.blanc@etu.univ-nantes.fr)*, **Bao Nhi Nguyen,** *Nantes Université, Univ Angers, Le Mans Université, CNRS, Laboratoire de Planétologie et Géosciences, LPG UMR 6112, France (baojulianguyen@gmail.com)*, **James A. Holmes,** *Sch. of Physical Sciences, The Open University, UK (james.holmes@open.ac.uk)*, **Brian Jackson,** *Dept. of Physics, Boise State University, IDA, USA (bjackson@boisestate.edu)*, **Lonneke Roelofs,** *Dept. of Physical Geography, Faculty of Geosciences, Utrecht University, the Netherlands (l.roelofs@uu.nl)*.

Introduction

Dust devils are transient convective vortices formed by solar heating of arid surfaces and resulting from superadiabatic lapse rates. They generate buoyant updrafts and rotating columns visible through lofted dust [1]. While terrestrial dust devils are typically under 100 meters tall, Martian counterparts can reach 2-8 kilometers due to lower gravity and a deeper boundary layer [1]. Martian dust devils contribute to a significant fraction of annual suspended dust (from 30 to 75% according to [9, 5]), modulating climate through albedo alteration and radiative forcing. Suspended dust in the atmosphere has been linked to influence on atmospheric water-ice nucleation [10]; as well as influence on oxydants production through the triboelectric effect [4]; which has been correlated with organic compound presence and methane destruction. The interest in dust devils also stems from their practical uses in lander missions, by removing dust from solar panels and extending lifespans of missions [1].

Here we leverage the data provided by Conway et al. [2] and their ≈14000 orbital detections (Fig. 2), and combine it with data from OpenMARS [6]and other remote sensing datasets. This study aims to establish environmental thresholds for Martian dust devil formation, such as terrain and atmospheric boundary layer constraints.

Initial datasets: Conway et al. [2] & OpenMARS

The detection and cataloguing of dust devils on Mars was accomplished by Conway et al. [2], using a RetinaNet Convolutional Neural Network, and data from the Context Camera (CTX) aboard the Mars Reconnaissance Orbiter (MRO), over Mars Years 28 to 36 at ≈6 m/px, spanning latitudes from 70°N to 70°S. The resulting detections were manually verified and resulted in 13 409 candidates.

From these detections were extracted multiple characteristics using Zooniverse: the brightest area of dust devil's plumes, a reference terrain not optically altered by the plumes and the path of dust devil's shadows (Fig. 1).

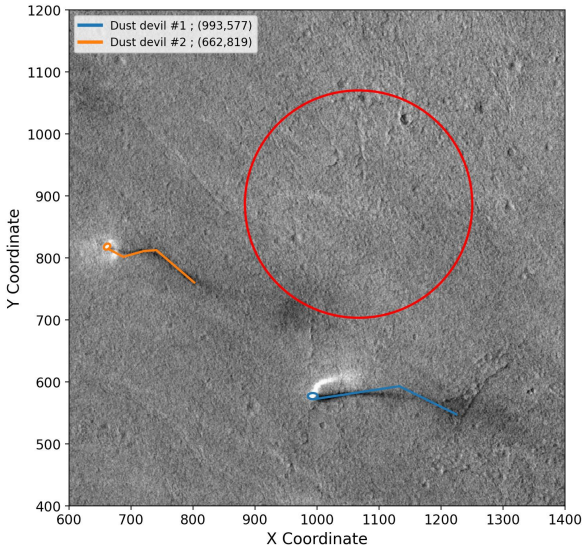

Figure 1: A Zooniverse annotation example, where the dust devil's bright plume is marked within an ellipse, and a line marks their respective shadows and a reference terrain is also outlined with a red circle. Coordinates are local pixel coordinates in a tile cropped from MRO's CTX image F18_042719_2155_XN_35N158W.

The Open access to Mars Assimilated Remote Soundings (OpenMARS) dataset combines spacecraft observational data with a Martian Global Circulation Model (GCM) [6].

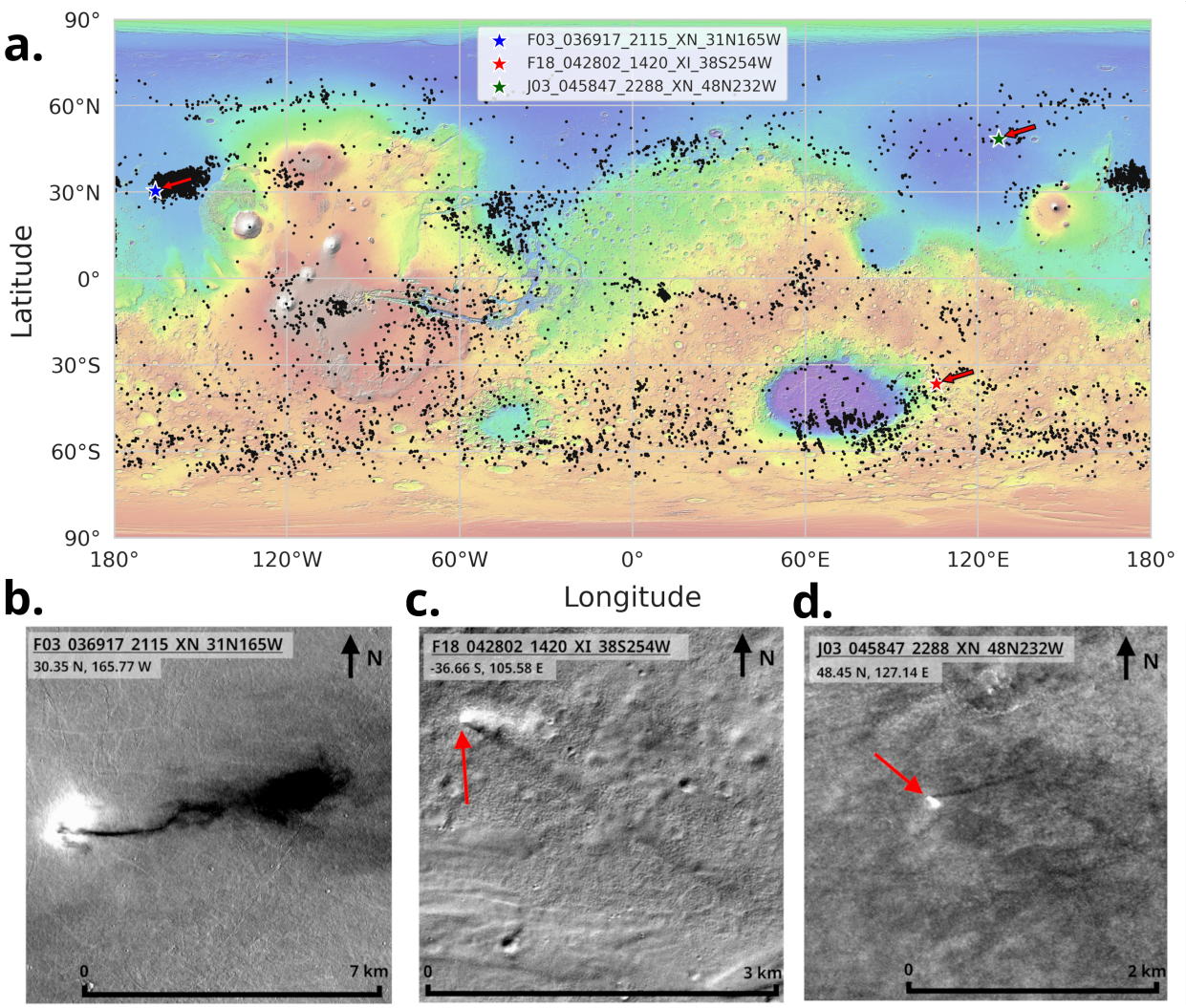

Figure 2: (a) Full dataset map from Conway et al. [2], with colourised and hill-shaded MOLA elevation map as background. Black points mark all confirmed dust devil detections; blue, red, and green stars indicate the locations of the three examples shown below. Below: CTX image tiles showing dust devil plumes (bright) and their shadows (dark). Red arrows mark the surface contact point. (b) dust devil in Amazonis Planitia, the tallest in the dataset; its shadow reveals a transition from dense plume to dispersed cloud. (c) dust devil near Avarua crater. (d) dust devil northwest of Elysium Mons.

OpenMARS provides hourly, gap-free global datasets of Mars' atmosphere and surface from Mars Years 24 to 32 [7]. For each CTX image with a dust devil in Conway et al. [2] we extracted temporal and atmospheric variables (MY, Local Time, Solar Longitude, wind speed, surface and near-surface temperature, and Planetary Boundary Layer height). We extracted terrain slope and the Dust Coverage Index (DCI) from the Mars Orbiter Laser Altimeter (MOLA), High-Resolution Stereo Camera (HRSC) Blended Digital Elevation Model, and the Thermal Emission Spectrometer (TES) Dust Coverage Index Map [15], respectively.

Methods: Height and relative reflectance

The dust devil's height was computed using the measured shadow length L from the Zooniverse data, the satellite emission angle e and the sun's incidence angle i (Eq.1) based on similar methods such as Corchete [3].

$$H_{DD} = \frac{L}{\tan(i) + \tan(e)} \tag{1}$$

By comparing the image brightness values of reference terrain, to the dust devil plume values (Fig. 1), we generated a relative reflectance where 0 indicates near transparency and 1 indicates an opaque plume.

Results and discussion

Atmospheric conditions The distribution of dust devil occurrences plotted as a density function over surface-air temperature difference and wind speed (Fig. 3) shows a well-bounded population. Data points are distributed between 0-27 m/s wind speed and 0-50 K temperature difference. The region of maximum density occurs at approximately 23 K and 8 m/s wind speed, suggesting optimal dust devil formation conditions. This reflects moderate convective instability and sufficient surface wind, consistent with prior studies [13, 8]. Higher values occur in the CTX data without dust devil detections, suggesting that above certain thresholds, conditions may inhibit vortex formation, possibly due to turbulence, disrupted rotation, or a shift toward dust storms. This aligns with Large-Eddy Simulation studies [11] showing optimal dust devil activity in moderate wind regimes (0-15 m/s).

Terrain conditions Dust devil height as a function of local slope shows a negatively skewed distribution (Fig. 4). The highest density of dust devils is found at 0° slope for dust devils of approximately 500 m in height. Around 50% of detections occur at slopes below 0.5°, and heights below 1500 m. While some dust devils are detected on slopes up to 10°, these are less frequent and are generally associated with dust devil heights below 1000 m. This relationship shows that steeper slopes generally limit vortex growth. Dust devils height decreases rapidly with increasing slope, where over 50% of dust devils occur on slopes <0.5°. Still, tall vortices (>2 km) occasionally occur on slopes up to 10°, suggesting steep slopes inhibit, but do not preclude tall vortex formation.

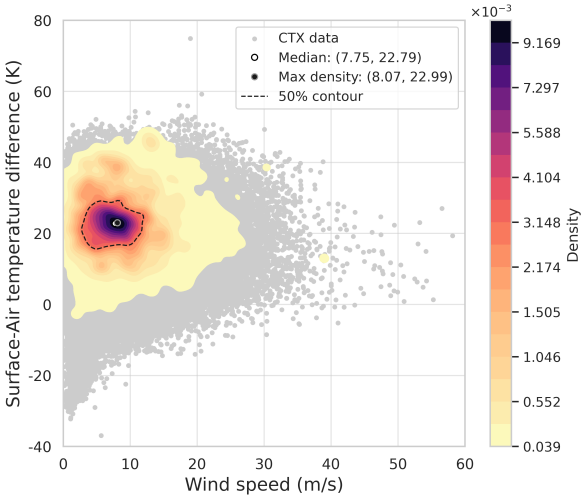

Figure 3: OpenMARS wind speed vs. surface-air temperature difference for dust devils. Color shows dust devil number density; grey points represent the full CTX dataset.

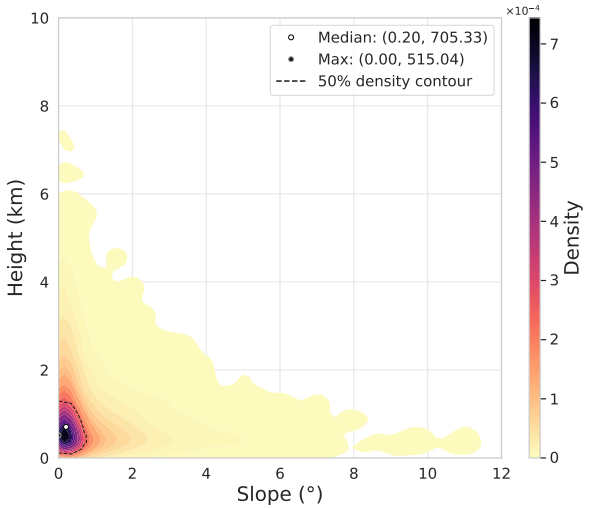

Figure 4: The influence of slope on dust devil height in our dataset.

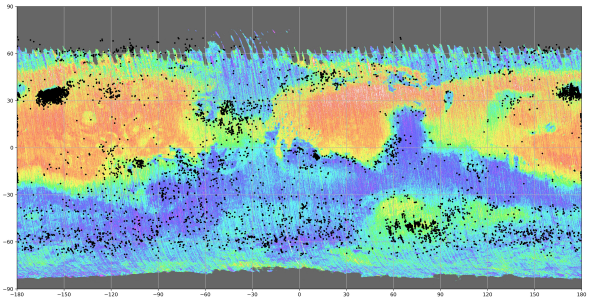

Figure 5: Dust devil detections (in black) over the TES Dust Coverage Index map of Ruff and Christensen [15] (Blue to red increasing the dust coverage)

While Renno et al. [14] proposed that slope-enhanced convection may promote dust devil formation along crater rims or ridges, our results suggest this effect is not a dominant mechanism. This interpretation aligns with the global dust devil track survey by Whelley and Greeley [16], which observed similar spatial distribution of dust devil tracks, with high density of dust devil tracks in flat terrain, losing density as the slope increases.

The spatial distribution shown in Fig. 5 reveals that most dust devils in the Northern Hemisphere occur in transitional boundary areas, typically around regions of high dust coverage index. In the southern hemisphere, low dust coverage is characteristic of the environment, with most dust devils concentrated near the latitudinal hotspot around 60°S. Examination of the global data (Fig. 6.a) shows that a medium dust index value of approximately 0.95-0.96 is the most commonly observed in the dataset. Previous studies [16, 12] reported that dust devil tracks are most commonly associated with medium DCI values, which aligns with our findings. However, when examining the data without monitored site influence, a trend toward lower dust cover emerges.

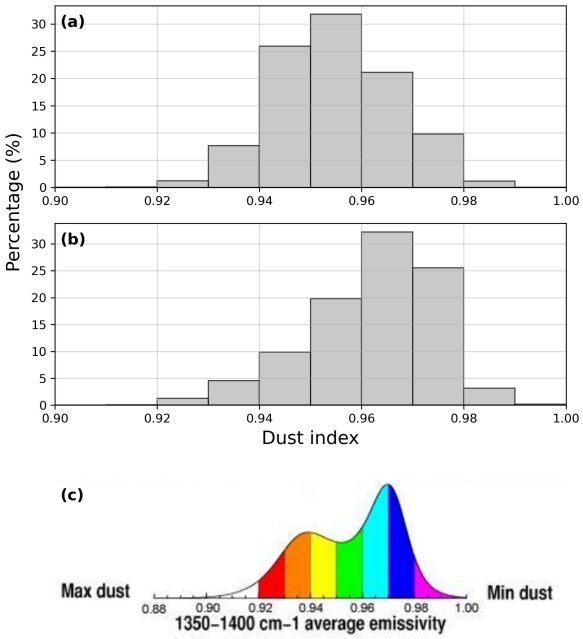

Figure 6: Histograms of dust devil detections TES Dust Coverage Index map of Ruff and Christensen [15], higher indicates lower dust coverage (and vice-versa). (a) a full dataset DCI histogram (b) the dataset DCI histogram without the monitored sites (Amazonis Planitia, Syria Planum, Meridiani Planum and Arcadia Planitia) and (c) the reference TES DCI global histogram

Similarly, both their results and ours show that areas with high dust coverage contain few dust devil tracks. Earlier interpretations suggested that fewer tracks in high dust coverage zones were due to increased dust deposition and a lack of bedrock exposure [12], and that low track density in low dust availability areas was due to insufficient material and a lack of albedo difference [16].

However, the current evidence suggests the scarcity of tracks in these regions to be primarily due to a lower frequency of dust devil occurrences. This is further supported by Fig. 6.b, which shows a skewness toward lower dust coverage. The DCI histogram in Fig. 6.c suggests that, when observation coverage is comparably dense, the overall distribution of DCI values may contribute to the observed preference for regions with lower dust coverage.

Conclusion

This study provides new constrains on atmospheric and terrain conditions linked to dust devil occurrences on Mars. We find that temperature differences of 23 K, wind speeds of 8 m/s, and flat terrain are more for dust devil formation. Medium levels of dust coverage are associated with a higher frequency of dust devil occurrences, reinforcing the connection between earlier research on dust devil tracks and the findings of this study. Our new dataset can be used to provide regional boundary conditions to help improve the representation of the Martian dust cycle within global climate models.

Acknowledgements

We are grateful for financial support from the French Space Agency CNES. We use data generated via the Zooniverse.org platform, development of which is funded by generous support, including a Global Impact Award from Google, and by a grant from the Alfred P. Sloan Foundation.

References

[1] M. Balme et al., 2006. 10.1029/2005RG000188.
[2] S. J. Conway et al., 2025. 10.1016/j.pss.2025.106072.
[3] V. Corchete, 2024. 10.1016/j.icarus.2024.116201.
[4] G. T. Delory et al., 2006. 10.1089/ast.2006.6.451.
[5] L. Fenton et al., 2016. 10.1007/s11214-016-0243-6.
[6] J. Holmes et al., 2019. 10.21954/ou.rd.c.4278950.
[7] J. Holmes et al., 2022. 10.21954/ou.rd.24981669.
[8] J. Ito et al., 2013. 10.1175/JAS-D-12-085.1.
[9] J. Koch et al., 2005. 10.1029/2005GL023420.
[10] F. Montmessin et al., 2002. 10.1029/2001JE001520.
[11] H. Ohno et al., 2010. 10.2151/sola.6A-002.
[12] D. Reiss et al., 2011. 10.1016/j.icarus.2010.09.009.
[13] N. O. Rennó et al., 1998. 10.1175/1520-0469(1998)055%3C3244:ASTTFD%3E2.0.CO;2.
[14] N. O. Renno et al., 2004. 10.1029/2003JE002219.
[15] S. W. Ruff et al., 2002. 10.1029/2001JE001580.
[16] P. L. Whelley et al., 2008. 10.1029/2007JE002966.